APPLIED SCIENCES AND ENGINEERING

Photothermally and magnetically controlled reconfiguration of polymer composites for soft robotics

Jessica A.-C. Liu[1], Jonathan H. Gillen[1], Sumeet R. Mishra[1], Benjamin A. Evans[2], Joseph B. Tracy[1]*

New materials are advancing the field of soft robotics. Composite films of magnetic iron microparticles dispersed in a shape memory polymer matrix are demonstrated for reconfigurable, remotely actuated soft robots. The composite films simultaneously respond to magnetic fields and light. Temporary shapes obtained through combined magnetic actuation and photothermal heating can be locked by switching off the light and magnetic field. Subsequent illumination in the absence of the magnetic field drives recovery of the permanent shape. In cantilevers and flowers, multiple cycles of locking and unlocking are demonstrated. Scrolls show that the permanent shape of the film can be programmed, and they can be frozen in intermediate configurations. Bistable snappers can be magnetically and optically actuated, as well as biased, by controlling the permanent shape. Grabbers can pick up and release objects repeatedly. Simulations of combined photothermal heating and magnetic actuation are useful for guiding the design of new devices.

INTRODUCTION

The field of soft robotics is rapidly expanding as soft robots are developed with new capabilities, designs, and materials (1–3). Soft robots have numerous applications, including biomedical and surgical tools (4), assistive healthcare devices (5), tissue engineering (6), and aerospace (7). Embedding stimulus-responsive particles in polymers can enable actuation of composites for use in soft robotics and impart complex functions. The behavior of most soft robots is responsive because they are composed of elastomers that lack hysteresis in their mechanical response. Responsive materials respond to applied stimuli and return to their initial shape in the absence of stimuli. Soft robots that exhibit sequential and programmable responses are desirable for performing complex functions and in remote environments, such as in vivo applications or space. Recently, there has been notable progress in making soft robots reconfigurable, where arbitrary configurations can be locked in place, followed by unlocking and reconfiguration (8, 9). It is also important to be able to program the configuration of a soft robot in the absence of stimuli. Thermally activated shape memory polymers (SMPs) are related to elastomers but are stiff at room temperature and become soft and elastomeric when heated, which allows setting a temporary shape (10). Heating can trigger an SMP to recover its permanent shape. Here, we report reconfigurable and remotely actuated soft robots using a commercial SMP with embedded commercial Fe particles with a diameter of 4 μm that are used in a bifunctional manner for simultaneous magnetic actuation and photothermal heating, simulate the responses and reconfigurability of these materials, and demonstrate simple soft robotic devices, including cantilevers, flowers, spirals, grabbers, and bistable snappers. This kind of soft robotic platform driven by a combination of magnetic field and light could be used to make programmable and reprogrammable soft robots for a wide range of applications.

SMPs are a broad class of materials that can be triggered by a wide range of physical and chemical stimuli. In this work, we have used a common one-way, thermally activated SMP, which consists of hard and soft components, where the soft component determines the transition temperature to create the temporary shape and the hard component prevents flow and defines the permanent shape above the transition temperature (11–13). The permanent shape is determined during processing of the polymer, typically by the shape of the mold used for melt processing or solvent casting. When a thermally activated SMP is deformed while heated above its transition temperature but below the melting or decomposition temperature of the hard component and cooled in the deformed configuration, it retains the new temporary shape. Reheating in the absence of any external constraints drives recovery of the initial permanent shape (10, 14–16). The permanent shape can also be changed by constraining the polymer in a new configuration while heating close to the melting or decomposition temperature of the hard component (17, 18). SMPs are thus an appealing material for soft robotics because temporary shapes allow shape fixity rather than requiring constant external simulation to maintain an actuated state, and the permanent shape can also be programmed (19).

While classical, one-way SMPs are widely available, a major drawback for using them in soft robotics is their lack of reconfigurability or cyclability without resetting a temporary shape by heating and applying mechanical constraints. An important branch of research on SMPs aims to develop two-way or reversible bidirectional shape memory that typically involves substantial chemical complexity (20–22). In this work, commercially available, one-way, thermally activated SMPs enable the creation of reconfigurable composites, where magnetic fields are used to set temporary shapes while illuminating the composite to drive photothermal heating and reduce the elastic modulus of the SMP. The temporary shape can be repeatedly locked and then subsequently unlocked and reconfigured. The device function can be further programmed by modifying the permanent shape, which can be used to bias actuation by controlling the elastic energies.

Magnetic and optical actuations are of great interest for soft robotics because they can impart complex responses and do not require electrical or pneumatic tethers (23–25). For example, assembling magnetic nanoparticles or microparticles into chains during embedding in elastomers or using ferromagnetic particles with substantial remanent magnetization can be used to program the response to

[1]Department of Materials Science and Engineering, North Carolina State University, Raleigh, NC 27695, USA. [2]Department of Physics, Elon University, Elon, NC 27244, USA.
*Corresponding author. Email: jbtracy@ncsu.edu

applied magnetic fields (24, 26–31). In photothermal heating, materials absorb and convert light into heat (32). Light also provides spatial control, and the amount of heat generated depends on the light wavelength, intensity, duration of illumination, and loading of absorbing species (33). Several materials have been used to trigger shape recovery of SMPs using photothermal heating, such as gold nanoparticles (14, 15, 25), carbon nanotubes (34, 35), and conducting polymers (36, 37), but these materials are not simultaneously magnetic. To the best of our knowledge, all of the SMP composites using photothermal heating solely perform shape recovery from a temporary shape to the permanent shape. With only one stimulus, reconfigurability remains challenging. Magnetic hyperthermia is a common approach for heating magnetic nanoparticles using alternating magnetic fields (AMFs), which can be used to trigger shape recovery of SMPs (12, 16). Magnetic hyperthermia usually involves an inductive heater consisting of conductive metallic coils cooled by chilled water to generate an AMF, which effectively serves as a large tether. Furthermore, application of a static magnetic field for magnetic actuation of a soft robot is not compatible with simultaneous application of an AMF. A related tethered approach that gives reconfigurability is a heterogeneous structure with segments that can be softened by Joule heating (38). Several recent studies have reported photothermal heating using magnetic nanoparticles for hyperthermia cancer therapy and driving reactions with large activation energies (33, 39, 40). Recently, the low Curie temperature of CrO_2 particles was used with photothermal heating to modulate the responsiveness of elastomers to applied magnetic fields (41). To the best of our knowledge, the use of magnetic particles to impart reconfigurability through simultaneous photothermal heating and actuation of SMPs has not been reported.

Actuation of these SMP composites is guided by the competition of magnetic, elastic, and gravitational energies. The applied magnetic field controls the magnetic energy, and the elastic energy depends on the part geometry, permanent shape, and temperature, which is controlled by photothermal heating and convective cooling. Snappers are a class of structures where there are multiple (often degenerate) elastic energy minima separated by elastic instabilities (9, 42–45). Applied forces drive snapping between different configurations. Small amounts of work can drive the system across an elastic instability, potentially resulting in a large mechanical deformation (46). Grabbers have the ability to hold onto objects and are vital tools in robotics, manufacturing, and surgery. Most of the previously reported soft robotic grabbers are electrically or pneumatically driven (47, 48). For example, octopus-inspired arms composed of cables and shape memory alloy springs can be electrically actuated (49), and a universal gripper based on granular materials contracts and hardens to pinch and hold an object upon application of a vacuum (50). A mechanism based on the response to magnetic fields or light is another simple way to control actuation (51–53). Simulations of the behaviors of soft robots are useful for their design and for understanding and optimizing their behaviors (54–56). Simulations in this work complement and corroborate experiments, and the simulation framework is useful for designing new devices that combine magnetic actuation with shape memory.

RESULTS AND DISCUSSION
### Material design and characterization
Fe microparticles [magnetic microparticles (MMPs)] were embedded into two types of thermoplastic polyurethane thin films: an SMP

(DiAPLEX MM5520), which requires heating for actuation, and an elastomer (IROGRAN PS 455-203). IROGRAN does not exhibit shape memory at room temperature and was used for comparison with the shape memory effects and reconfigurability of DiAPLEX. Several parameters for the design of these materials were chosen because of the commercial availability of these materials and based on our recent work, including the use of 4-μm Fe particles that have high saturation magnetization and lack magnetic hysteresis, a loading of ~10 weight % (wt %) for most experiments, and device dimensions of a few centimeters laterally and ~100 to 300 μm thick (25, 27, 28). A light-emitting diode (LED) was used for photothermal heating of the MMPs embedded in DiAPLEX to reduce its modulus and allow actuation with applied magnetic fields. Thus, the structures obtained through magnetic actuation can be locked into temporary shapes at room temperature after switching off the LED and removing the magnetic field. The structures can be reconfigured by turning the light back on to drive shape recovery to the permanent shape in zero magnetic field or by simultaneously applying the magnetic field in a different direction to cause reshaping. Fe particles absorb light of many different wavelengths, and 860 nm was chosen for this study because we recently used the same LED for photothermal heating of gold nanorods in DiAPLEX (25). Thin films of DiAPLEX and IROGRAN containing embedded magnetic particles were prepared by solvent casting. Cantilever, scroll, and snapper devices with chained magnetic particles were prepared by solvent casting in an electromagnet with a uniform, horizontal field of 150 Oe, which drives magnetic field–directed self-assembly of the magnetic particles into chains (28, 57).

The structure and the thermomechanical, optical, and magnetic properties of the polymer composites were characterized (figs. S1 to S3), and the temperature dependence of the elastic modulus and magnetic properties of the loaded DiAPLEX and IROGRAN samples were used as inputs for modeling. Measurements of the glass transition temperature (T_g) of loaded DiAPLEX are quite close to blank DiAPLEX, with values ranging from 43° (by differential scanning calorimetry) to 55°C (peak of tanδ in dynamic mechanical analysis measurements). The elastic modulus is slightly higher for the loaded DiAPLEX sample below T_g and quickly decreases at T_g, as expected. Loading the IROGRAN sample also increases its elastic modulus at 25°C. Imaging by scanning electron microscopy shows accumulation of the Fe particles toward the bottom of the film due to gravity. The films have a broad extinction spectrum, which is consistent with their gray appearance, although considerable scattering is also expected from the Fe particles. Magnetization curves of the composites have a sigmoidal shape characteristic of soft Fe particles that lack coercivity and were used as an input for modeling. Details of the structure of the chains and their effects on the magnetization behavior and actuation have already been discussed in our previous reports (27, 28).

Cantilever experiments
The concept of combining photothermal heating and magnetic actuation of SMPs with embedded Fe particles was first demonstrated in a cantilever experiment (Fig. 1). When a rectangular strip of the SMP film with magnetic chains oriented along the length is anchored to the substrate on its right side, with a permanent magnet held at a fixed height above the left side of the cantilever, it does not lift because the elastic energy associated with bending at room temperature is too high to allow bending. After switching on the LED for 7 s, photothermal heating of the magnetic particles causes heating and softening of the surrounding DiAPLEX matrix, thus reducing the elastic energy and allowing the cantilever to bend and lift toward the permanent
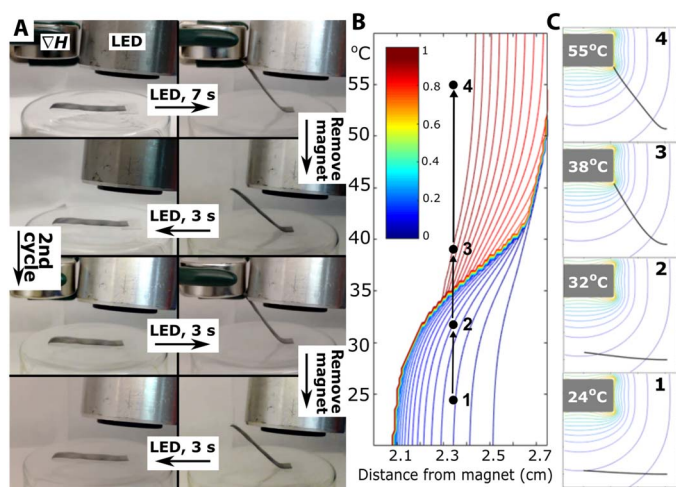
Fig. 1. Shape memory cantilever containing chained magnetic particles. (**A**) Actuation and (**B** and **C**) simulations of a DiAPLEX cantilever film containing chained magnetic particles. The permanent magnet (∇H) and LED are indicated in the top left panel. (B) The contours show the degree of actuation (0, flat; 1, contacting magnet) of a simulated filament across a range of positions and temperatures. (C) Simulated still images correspond to discrete points along the path indicated in (B), at a distance of 2.3 cm from the magnet, which is consistent with the experimental geometry on the left. See movies S1 and S2 for experiments and simulations of the cantilever. Photo credit: Jessica A.-C. Liu, North Carolina State University.

magnet. Switching off the LED and removing the magnet freezes the cantilever in the lifted position, again because of the high elastic energy associated with bending DiAPLEX below its glass transition temperature. Turning the LED on for 3 s without the magnet caused the elevated cantilever to return to its initial flat position. In a second lifting cycle, the cantilever lifted after illumination for only 3 s because of residual heat in the cantilever from the first lifting cycle. Therefore, magnetic actuation coupled with photothermal heating enables multiple cycles of locking and unlocking soft robots, for which 10 cycles, including thermal imaging, are recorded in movie S3. Placement of the video and thermal imaging cameras is shown in fig. S4.

Modeling cantilevers
Actuation of the cantilever was reproduced in silico with a custom finite-element model implemented in MATLAB. A cantilever with dimensions of 3.0 cm by 0.5 cm by 130 μm was fixed at one end, and a permanent NdFeB magnet ($d = 2.5$ cm, $l = 1.25$ cm) was located with its face 2.3 cm from the plane of the resting cantilever. Magnetic gradient, elastic, and gravitational forces were included in the simulation. In general, a high–aspect ratio magnetic material will experience both a magnetic torque that tends to align it with an applied field and a magnetic force that pulls it upward along an applied field gradient. The magnetic torque per unit volume is given by $\vec{\tau} = \vec{M} \times \vec{B}$, while the magnetic force per unit volume is $\vec{F} = \nabla(\vec{M} \cdot \vec{B})$, where M is the magnetization per volume (A/m) and B is the magnetic flux density (T). Comparing the respective energies over a small rotation, θ, we find $U_\tau \sim MB\theta$ and $U_F \sim M \nabla B \theta L$, where L is a characteristic length of the structure. The ratio of energies due to magnetic forces and magnetic torques is therefore given by $U_F/U_\tau = \nabla B L/B$. From measurements of the magnetic field along the path followed by the tip of the 3-cm cantilever, we find that at all points along that path,

$\nabla B/B \approx 140$ m^{-1}, yielding an energy ratio of $U_F/U_\tau \geq 4.2$. Furthermore, this energy ratio is for a limiting case, where the induced magnetic moment of MMPs in the filament is always aligned with the axis of the filament. Any deviation from this alignment will further increase the ratio, U_F/U_τ. Thus, magnetic forces due to field gradients are the dominant influence, and magnetic torques are omitted from our simulations. As the temperature increased, the temperature-dependent modulus of the DiAPLEX filament decreased, diminishing the influence of elastic energy in favor of magnetic energy and resulting in net motion toward the magnet. In our simulations, the magnetic susceptibility of the filament is obtained from fits to magnetometry measurements (fig. S1), which incorporate the effects of chaining the MMPs. This motion is represented in still frames in Fig. 1, and movie S2 includes simulations of shape recovery.

Actuation of the filament is rapid, because magnetic forces increase as the filament approaches the magnet. To visually represent the sharpness of the transition between resting and completely actuated states and explore a wider expanse of the relevant parameter space, we simulated the equilibrium position of the filament across a range of magnet positions and filament temperatures. Under each condition, the "degree of actuation" was determined by taking the ratio of the vertical position of the magnet face divided by the vertical position of the tip of the filament. Thus, a flat horizontal cantilever would represent zero actuation, while a filament in contact with the magnet face would present a degree of actuation of one. The degree of actuation is plotted in the contours in Fig. 1. In this figure, the space between consecutive contours represents a 1.5% difference in the degree of actuation, and the vast majority of cantilever movement (~80%) is seen to occur during a single step in either the magnet position ($\Delta y = 0.1$ mm) or temperature ($\Delta T = 0.5°$C). Parameter-space plots such as these highlight the utility of the simulation for predicting the behavior of devices across a broad range of conditions.
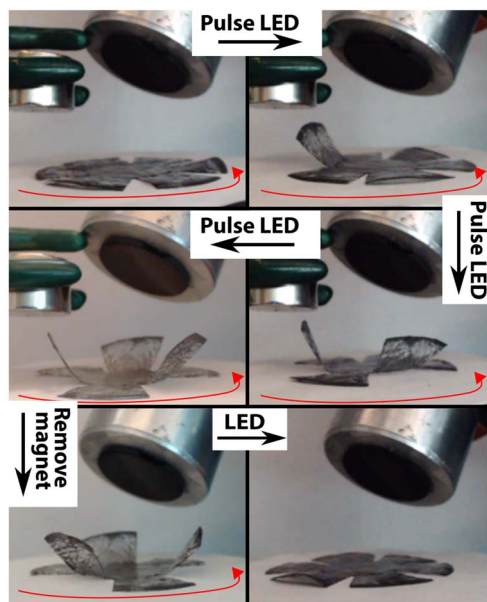
Comparison of experiment and modeling
Computational modeling is a powerful tool aiding and accelerating the design of new soft robots by allowing their construction, testing, and optimization in silico. A detailed computational model may be further used to validate a set of simple and broadly applicable scaling relationships, which can be used to predict behavior and optimize design. These relationships are discussed later in this paper. It is important that the computational model agrees with experimental outcomes, and throughout the article, we have shown that the simulated devices, operating under the assumptions described above, do closely match with experimental results. An important consequence of the dominant role of translational forces due to field gradients, as opposed to magnetic torques, is that the location of the Fe particles across the thickness of the film is not expected to affect the force per unit length and therefore should not influence actuation. While we noted from scanning electron microscopy (fig. S2) that the Fe particles are more concentrated in the bottom of the film because of gravitational settling during the solvent casting process, the nonuniformity is not expected to affect the actuation behavior.

An important source of disagreement between experiment and modeling is the temperature profile in the film during photothermal heating. The spot from the LED is not uniform and produces a hot spot in the film that is observed in thermal imaging (fig. S4 and movie S3), while modeling assumes a uniform temperature throughout the film. Quantitatively addressing this issue is beyond the scope of this study and would involve a more complicated light source or

modeling of the temperature profile and associated thermal transport. From thermal imaging, an illumination intensity exceeding 33 mW/cm^2 is required for actuation, and at the intensity of 154 mW/cm^2 used in these experiments, the cantilever lifts when the center of the hot spot reaches 43°C, while lifting in the simulations occurs when the temperature of the film reaches 38°C. It is reasonable that modeling would predict a lower uniform temperature for actuation than the hottest point measured in the experiment that is surrounded by cooler regions that will resist actuation. Incorporating point-source heating and thermal transport within the simulation would enable more precise predictions for specific illumination schemes but would significantly increase the complexity of the simulations while reducing their broader applicability for informing the design of generalized devices.

Flowers

By changing the shape of the polymer film, flowerlike robots were constructed with petals that can be reconfigured when simultaneously exposed to a magnetic field and illuminated. The particles in this sample were not chained because of the radial sample geometry. As the flower laid flat and was rotated, the petals first passed beneath the LED for heating, causing them to lift when they next rotated beneath a permanent magnet. All the petals lifted up in sequence and remained lifted because they cooled and stiffened while held up by the permanent magnet. After removing the permanent magnet with the LED switched off, the petals remained locked in the up position. After turning the LED on again, the petals softened and returned to the original down position (see fig. S5 for the actuation of a DiAPLEX flower film with eight petals containing unchained magnetic particles). Photothermal heating with the LED can be further used to optically select

which petals lift. If the LED is pulsed on and off as the flower rotates beneath the magnet, then every other petal is illuminated, heated, and lifted, while the remaining petals do not move (Fig. 2). Removing the magnet and illuminating for a full rotation of the flower returns all of the petals to their flat starting position.

Scrolls

We present a reconfigurable scroll that can be opened, locked, reset to the closed configuration, and then opened again. Strips of DiAPLEX and IROGRAN with magnetic particles chained along their length were rolled around a glass pipette by hand, followed by heating to 180°C for 6 hours and 80°C for 30 min, respectively, while clamping the scroll closed, to set the closed position as the permanent shape. The IROGRAN scroll behaves as an elastomer at room temperature; a permanent magnet can be used to pull the scroll open, and then it snaps closed when the magnet is pulled away (Fig. 3A). The outer end of the scroll was affixed to a nonmagnetic support. As the permanent magnet was moved toward the scroll and retracted, the attractive magnetic force caused the scroll to extend and unroll. After fully extending the scroll, pulling the magnet further away reduced the magnetic force, and the scroll abruptly closed. The same principle was investigated using DiAPLEX, for which simultaneous illumination with the LED was required for reconfiguration and also allowed the scroll to be locked open or closed indefinitely (Fig. 3B). After removing the magnet, illuminating the open scroll caused it to return to its closed, permanent shape.
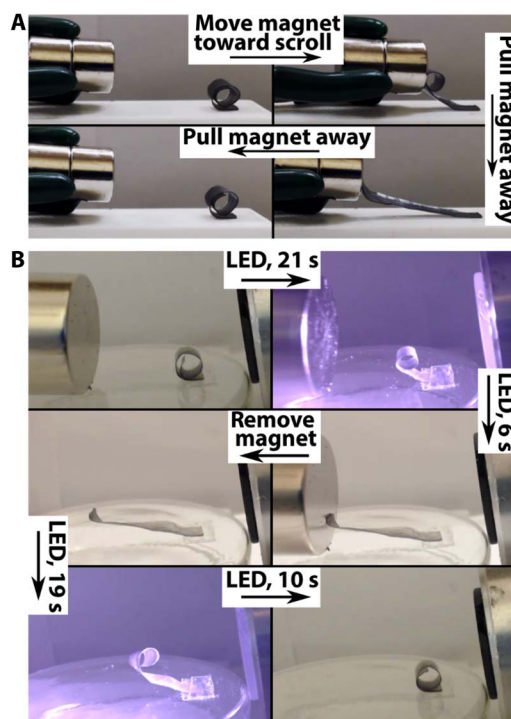

Fig. 2. Rotation of a shape memory flower while pulsing the LED. Rotation of a DiAPLEX flower with six petals containing unchained magnetic particles counterclockwise beneath the LED first causes photothermal heating and softening of the petals, followed by lifting beneath the permanent magnet. Switching the LED on and off allows heating and lifting of every other petal. A video of this experiment is presented in movie S4. Photo credit: Jessica A.-C. Liu, North Carolina State University.

Fig. 3. Magnetic scrolls. (**A**) Actuation of an IROGRAN scroll by moving the magnet toward the scroll and pulling the scroll open. The scroll abruptly closes when the magnet is pulled further away. (**B**) Actuation of a DiAPLEX scroll placed next to a permanent magnet with illumination by a LED. Turning off the LED and removing the magnet locks the open configuration. Removing the magnet and turning on the LED causes the scroll to close. Videos for these experiments are presented in movies S5 and S6. Photo credit: Jessica A.-C. Liu, North Carolina State University.

Snapper experiments

Snappers were designed to investigate magnetically and photothermally triggered snapping using strips with embedded magnetic particles chained along their length in IROGRAN and DiAPLEX that were anchored to a three-dimensional (3D)–printed frame in a buckled configuration (8, 43, 47). The permanent shape of the composite film can also be used to program whether the snapper is biased toward one side by setting that buckled configuration as the permanent shape or unbiased by using the flat shape as the permanent shape. All four possibilities were investigated using biased and unbiased IROGRAN and DiAPLEX films.

In the unbiased IROGRAN snapper, a permanent magnet was applied to pull the strip through the elastic instability and into the opposing buckled configuration (Fig. 4). Because the two stable states were symmetrical, the force provided by the magnetic field gradient pulled the strip through the elastic instability. In the biased IROGRAN snapper, whose permanent shape is buckled to the right, moving the frame toward the permanent magnet drove snapping to the left. Upon moving the frame away from the permanent magnet, snapping to the right occurred spontaneously, and the permanent shape was recovered.

For DiAPLEX snappers, simultaneous illumination with the LED was required to soften the polymer and sufficiently reduce the elastic energy to allow snapping, which occurred within 3 to 5 s of illumination (Fig. 5). After switching off the LED and removing the magnet, the film remained buckled to the left for both the unbiased and biased snappers. In the snapper biased with buckling to the right as the permanent shape, illumination without the magnet drove shape recovery by snapping back after 17 s (Fig. 5B). The biased DiAPLEX snapper used higher loadings of MMPs to enhance its response to the magnetic field and a shorter length than the unbiased DiAPLEX snapper to increase the uniformity of illumination by reducing the angle between the LED and the ends of the snapper. For the unbiased DiAPLEX snapper, rotating the sample frame 180° along the vertical axis to switch the orientation of the device with respect to the magnet and LED allowed repetition of the experiment, which drove snapping back to the initial configuration. These experiments demonstrate that the concept of coupling temperature-dependent elastic modulus, magnetic actuation, shape memory, and photothermal heating can be used to program the behavior of snappers.

Modeling responsive snappers

In the simulations shown in Fig. 4, IROGRAN snappers are modeled as 4.8 cm by 0.5 cm by 252 µm filaments cantilevered at both ends. The spacing between the ends is set at 4.0 cm to match the experimental geometry, and the filament is allowed to relax to a buckled equilibrium conformation with stored elastic energy. For simulations using IROGRAN, the temperature is not varied, and a constant value (23 MPa) is used for the elastic modulus. The field from a cylindrical permanent magnet (d = 2.5 cm, l = 1.25 cm) is simulated, and the magnet is moved relative to the fixed frame supporting the filament to reproduce experimental conditions. Gravitational forces are neglected in simulations of the snappers; the equilibrium configurations shown result solely from the elastic and magnetic energies, which are calculated in the same way as for the cantilevers. In the unbiased IROGRAN simulation, the filament snaps symmetrically through its elastic energy barrier
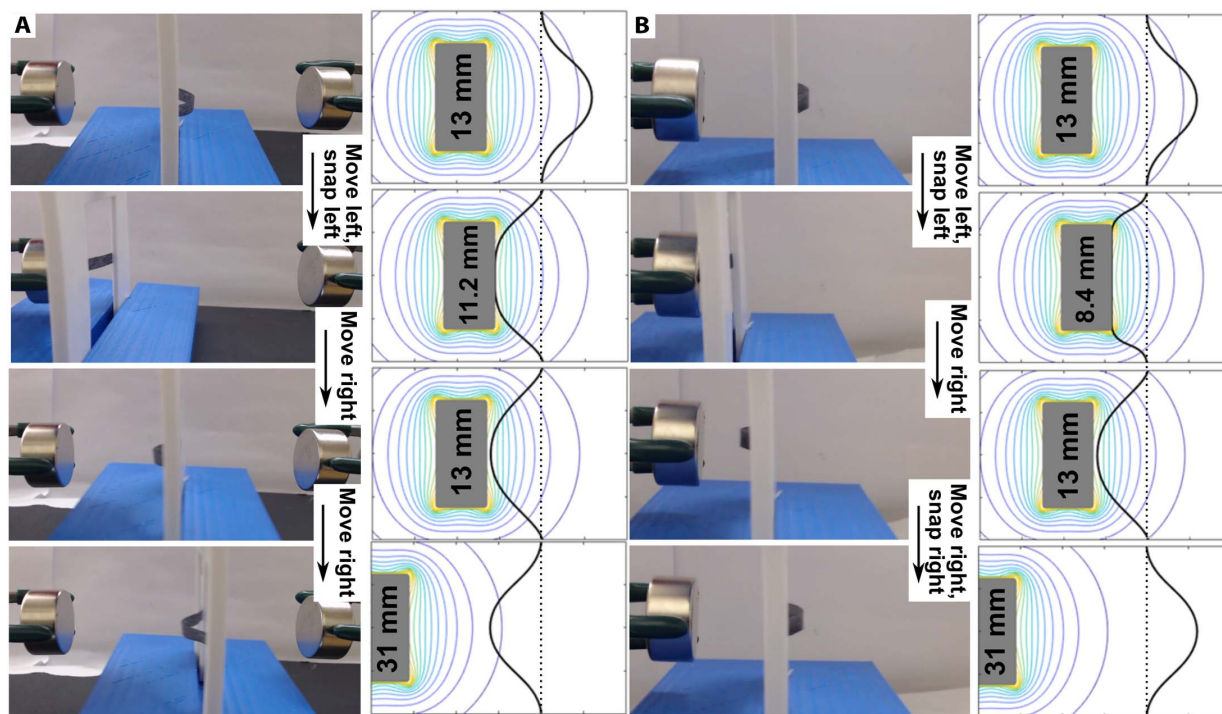
Fig. 4. Unbiased and biased elastomer snappers. (**A**) An unbiased IROGRAN snapper containing magnetic particles chained along its length is placed between two permanent magnets. When moving the frame supporting the snapper closer to one magnet or the other, snapping occurs to pull the buckled direction toward the magnet. Moving the sample to the left and right causes repeated, reversible snapping. (**B**) Biased IROGRAN snapper containing magnetic particles chained along its length. Moving the frame closer to the magnet causes snapping toward the magnet. When moving the frame away from the magnet, snapping occurs away from the magnet and back into the favored direction set by biasing. The simulations closely match experiments, and videos are presented in movies S7 to S10. Photo credit: Jessica A.-C. Liu, North Carolina State University.
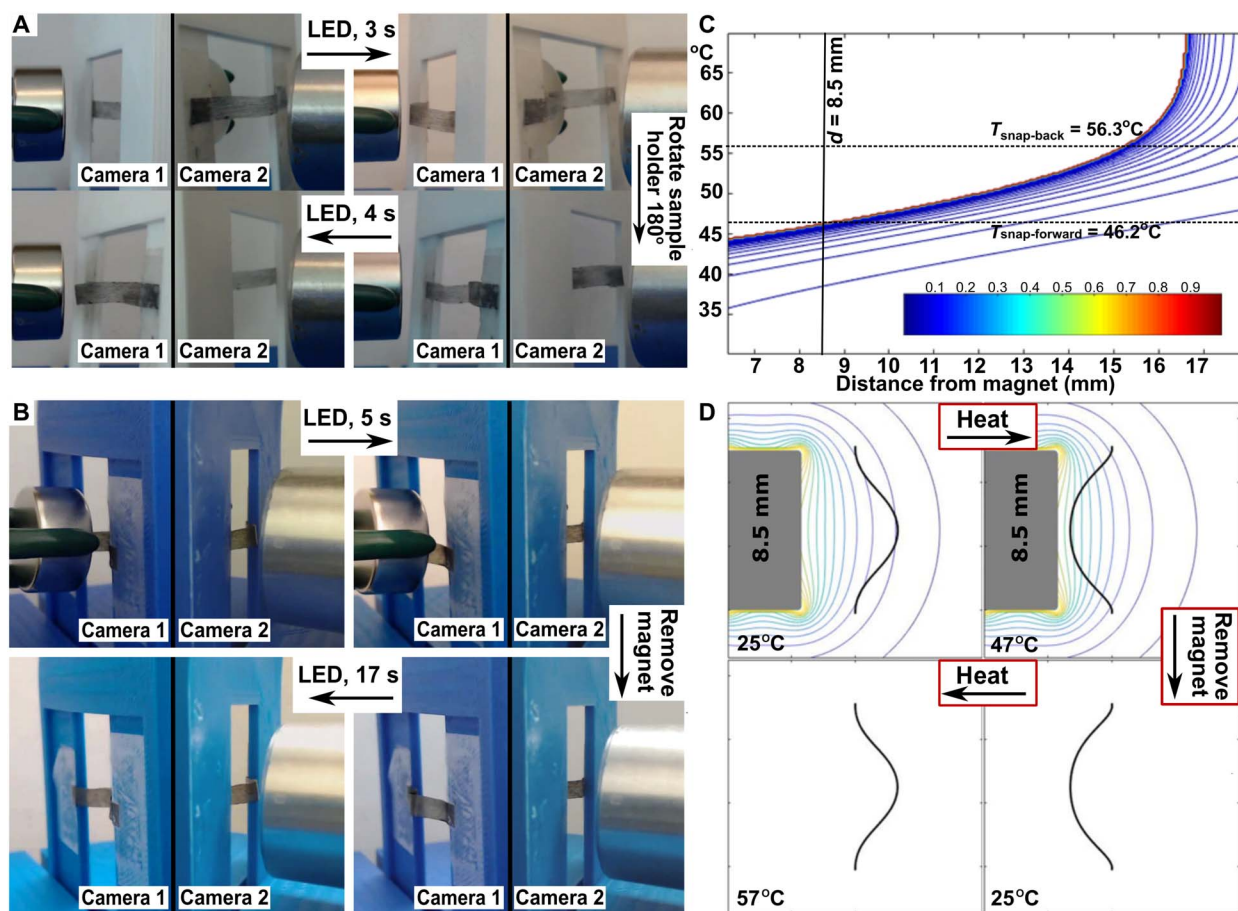
Fig. 5. Unbiased and biased shape memory snappers. Actuation of DiAPLEX snappers containing chained magnetic particles with Camera 1 and Camera 2 positioned on both sides of the snapper. Camera 1 and Camera 2 show the sides with the permanent magnet and LED, respectively. Placement of the cameras and the snapper is shown in fig. S6A. (**A**) The unbiased snapper has a flat permanent shape. Turning on the LED triggers snapping toward the magnet, which is repeated when the sample is turned around. (**B**) The permanent shape of the biased snapper is buckled toward the LED. (**C**) Summary of simulations for a biased snapper, where the contour lines (drawn at 0.5% intervals) indicate the dependence of the degree of snapping on temperature and the distance from the magnet. The same plot for an unbiased snapper is presented in fig. S7. (**D**) Simulations of the biased snapper correlate well with experimental observations. The simulations closely match experiments, and videos are presented in movies S11 to S14. Photo credit: Jessica A.-C. Liu, North Carolina State University.

when the magnet approaches to within 11.2 mm of the filament plane (Fig. 4A, dotted line). After removing the magnet, the filament remains in this secondary, "snapped" configuration, which is a mirror image of its original relaxed state. To simulate the biased IROGRAN snapper (Fig. 4B), the 4.8-cm filament is first buckled and allowed to relax to equilibrium in a 3.0-cm gap, and the resulting configuration is set as the new zero-energy, "biased" elastic state. Any deformations from the biased configuration will thus result in an elastic restoring force. The asymmetry of this biasing causes the filament to resist snapping until the magnet is closer than in the unbiased case (8.4 mm versus 11.2 mm) and to snap back into its original configuration after retracting the magnet. In the simulation, the return snap occurs at a magnet distance of 30.6 mm. For both the biased and unbiased IROGRAN snappers, the simulated snap and return-snap distances closely match the experiments.

Modeling reconfigurable snappers

DiAPLEX snappers are modeled with a smaller filament (2.9 cm by 0.5 cm by 142 μm) cantilevered across a gap of 2.5 cm. The biased and unbiased DiAPLEX snappers are modeled as biphasic materials with a "permanent" low-modulus (9.0 MPa) phase with a fixed equilibrium

conformation and a "temporary" phase with a temperature-dependent modulus (0 to 890 MPa). The equilibrium conformation of the temporary phase can be reset at any configuration by cycling the temperature. In the unbiased DiAPLEX snapper, the permanent configuration is flat, while in the biased DiAPLEX snapper, the permanent configuration is set in the biased equilibrium configuration that results from allowing the filament to relax across a 1.5-cm gap without a magnetic field. In simulations of biased DiAPLEX snappers (Fig. 5, C and D, and movie S14), the position of the magnet was fixed at 8.5 mm from the plane of the filament to match experimental conditions, and the temperature was increased. At 46.2°C, the decreasing elastic energy is overcome by magnetic energy, causing the filament to snap. The filament is then cooled to 25°C in the presence of the magnet to set the new temporary configuration, and the magnet is removed. The filament maintains its buckled configuration. Subsequently, heating the filament to 56.3°C results in a return snap into the original configuration.

The same system was simulated across a range of magnet distances and filament temperatures. The contours in Fig. 5C represent the "degree of snapping," which is defined as the fractional position of the center of the filament between the two fully buckled positions, with a

value of 0 in the rightmost position and a value of 1 in the leftmost position. The transition is extremely sharp; more than 90% of the movement occurs within a single step in magnet distance ($\Delta y = 0.05$ mm) or temperature ($\Delta T = 0.25°C$).

Grabbers

Soft robotic grabbers have potential for a wide range of applications. For example, pneumatic grabbers are well suited for food picking and packing to reduce labor costs and increase sanitation (58). Traditional rigid grabbers may damage soft foods and are limited in their abilities to reliably pick up deformable, soft objects. Here, we demonstrate a soft robotic grabber that remotely picks up and drops small pieces of fruit, blueberries and cherry tomatoes, weighing up to 20 times the weight of the grabber. This demonstration highlights the potential for in vivo applications because no tether is required, and the capability for remote actuation surpasses that of current implantable elastomers and SMPs (59).

Two related methods were used for loading objects in the grabber. In the first method, "magnet-assisted," the object rests on top of a permanent magnet. After the open grabber is lowered so that the open arms surround the object, turning on the LED softens the film, and the arms are pulled closed by the magnet (Fig. 6A). Switching off the LED then locks the grabber in the closed, temporary shape, allowing the object to be picked up and transported. Turning the LED on again after transporting the object away from the magnet causes the grabber to open and release the object into a collection container. A drawback of the magnet-assisted method is the required placement of the object on top of the magnet to close the grabber around the object, which could limit the applicability of this grabber. Furthermore, the presence of the object within the gripper impedes the arms from completely closing around the bottom of the object, which restricts the maximum weight the grabber can carry.

A second method, "push-through," uses the same grabber and addresses the limitations of the magnet-assisted method (Fig. 6B). The temporary shape of the grabber is preset by placing it above the magnet and turning on the LED to pull the arms closed. The magnetic field and its gradient control the displacement of the arms of grabber, and the final shape is determined by the balance of magnetic and elastic inter-actions. After switching off the LED, we brought the closed grabber to the object and picked it up by pushing it through the closed arms. The push-through method removes the requirement for placing the object on top of the magnet. Furthermore, the carrying capacity for the push-through grabber is also increased because the temporary shape of the arms is more tightly closed when they are not blocked by the object that is to be picked up. Release of the object from the push-through grabber is identical to the magnet-assisted method, where illumination with the LED opens the grabber and drops the object.

Design considerations for magnetic SMP devices

The numerical model can be directly applied to predict the detailed behavior of new devices, for example, in modeling a series of cantilever devices using SMPs with a range of glass transition temperatures offset by increments of 10°C (movie S17). Furthermore, having validated the assumptions of our computational model against experimental measurements for cantilevers and snappers, we can now generalize our model for developing useful and broadly applicable scaling relations to inform the design of magnetic SMP devices in gradient-dominated field geometries such that full simulations are not always required. The following formulas are derived in the Supplementary Materials. Assuming a uniform curvature for a length of SMP filament, we can approximate the elastic torque as a function of deflection angle as $\tau_E = (wt^3/3L)E\theta$. Furthermore, by assuming a uniform field and field gradient along the length of the filament, we can approximate the magnetic torque as $\tau_M = \frac{1}{2}wtL^2(\frac{\chi}{\mu_0}B + M)\nabla B$. In these expressions, w, t, and L are the width, thickness, and length of the filament, respectively; E is the elastic modulus; and θ is the deflection angle as defined in fig. S9. The dimensionless susceptibility $\chi = \mu_0\frac{\partial M}{\partial B}$ and the volume magnetization M are functions of the applied flux density B, and ∇B is the magnetic field gradient in the direction of deflection. Thus, at low field, where χ is approximately constant and $\mu_0 M \approx \chi B$, the term in parentheses reduces to $2\chi B/\mu_0$. At saturation, $\chi \to 0$ and the same term reduces to M_{sat}. Further details are available in the Supplementary Materials.

In general, an actuator will be at rest at an equilibrium position, where $\tau_E = \tau_M$, and motion is achieved by manipulating either elastic or magnetic torque to shift the equilibrium position. However, there
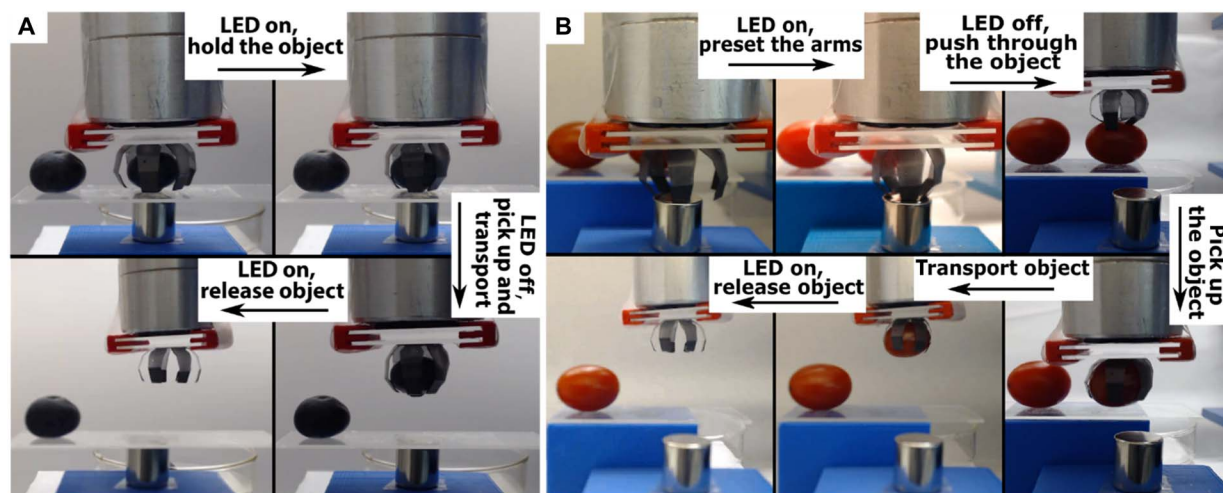
Fig. 6. Shape memory grabber picking up, transporting, and releasing small objects. (**A**) Blueberries (~1.5 g) using the magnet-assisted method (movie S15) and (**B**) cherry tomatoes (~3.2 g) using the push-through method (movie S16). The mass of the grabber is 152 mg. Photo credit: Jessica A.-C. Liu, North Carolina State University.

exists a notable tipping point in many geometries at which the rate of change in magnetic torque with displacement outpaces the rate of change in elastic torque. At this point, the degree of actuation becomes effectively infinite until halted by a mechanical impediment, such as contact with the magnet. This regime is described by $d\tau_M/d\theta > d\tau_E/d\theta$, and the "snap" transition at the onset occurs when $d\tau_M/d\theta = d\tau_E/d\theta$. Differentiating the torques presented above, we obtain the snapping condition, which is directly applicable under the approximations described above and more broadly predictive otherwise

$$\frac{\chi}{\mu_0}[B\nabla^2 B + (\nabla B)^2] = \frac{Et^2}{3L^4} \quad (1)$$

Further details of this derivation are available in the Supplementary Materials.

This simple relation predicts the circumstances of snapping, which we observe in both our cantilever and bistable snapper devices. Furthermore, it provides a clear set of scaling considerations that can be used to guide the design of snap-type actuators. Applied to our own simulated systems, we find that our DiAPLEX cantilever ($L = 3$ cm, $t = 130$ μm, $\chi = 0.075$, $B = 0.057$ T, $\nabla B = 5.2$ T m^{-1}, $\nabla^2 B = 590$ T m^{-2}) would be expected to snap when the elastic modulus reaches 520 MPa. In our detailed simulation, the transition occurs at a temperature of 34.2°C, which corresponds to a modulus of 520 MPa (movie S2). We see similar agreement in our bistable snapping devices. For the unbiased DiAPLEX snapper ($L = 2.4$ cm, $t = 120$ μm, $\chi = 0.075$, $B = 0.037$ T, $\nabla B = 3.1$ T m^{-1}, $\nabla^2 B = 315$ T m^{-2}), the relation predicts a snap at a modulus of 88 MPa, whereas snapping occurs in the simulation at a temperature of 45.1°C, corresponding to a modulus of 65 MPa (movie S12). In the unbiased IROGRAN snapper ($L = 2.4$ cm, $t = 252$ μm, $\chi = 0.075$, $E = 23$ MPa), snapping would be expected when $B\nabla^2 B + (\nabla B)^2 = 24$ T^2 m^{-2}. Snapping in the full simulation occurs at a distance of 11.2 mm (Fig. 4 and movie S8) when the apex of the filament is 22 mm from the face of the magnet, which corresponds to $B = 0.047$ T, $\nabla B = 4.0$ T m^{-1}, and $\nabla^2 B = 450$ T m^{-2}, or $B\nabla^2 B + (\nabla B)^2 = 37$ T^2 m^{-2}. The differences between the expectations from Eq. 1 and results from simulation are consistent with the extra elastic energy associated with buckling in the snapper devices. Note that the relevant length scale in the snapper devices is the half-length of the snapper, which is used in all calculations above.

Thus, a central aspect of our detailed simulation can be effectively encapsulated in a simple, useful, and broadly applicable expression. Applying this predictive power, we can use Eq. 1 to anticipate the performance of magnetic SMP devices outside the range of our experiments. For example, as noted above, our unbiased DiAPLEX snapper snaps at a modulus of about 65 MPa (45.1°C). Recognizing that the modulus of the DiAPLEX drops to about 9 MPa at 80°C, the simple scaling in Eq. 1 would predict a failure to snap at even this lowest modulus if χ falls below 0.01. Assuming a linear relationship between the Fe loading and χ, this would correspond to a loading of 1.3 wt %. Running the full simulation for different loadings indicates that while the unbiased DiAPLEX snaps at 1.4 wt % loading, it fails to snap at 1.3 wt % loading. When decreasing the loading, the absorption of light could also decrease, which might need to be compensated by an increase in the illumination to achieve sufficiently high temperature for actuation. Using Eq. 1, we can also predict that doubling the thickness of our DiAPLEX cantilever would reduce the modulus required for a snap by a factor of 4, from 520 MPa (34°C) to 130 MPa (42°C). Using the full simulations, we have further con-

firmed that this is precisely the modulus at which snapping occurs for a cantilever of twice the thickness.

For SMP actuators operating below this tipping point, the deflection θ occurs at an equilibrium position where $\tau_E = \tau_M$ and thus ranges between the two prominent equilibria defined by its highest modulus (τ_E evaluated at E_H) and lowest modulus (τ_E evaluated at E_L), depicted in fig. S9. Taking the difference in deflection between these extrema yields an expression for the range of motion of the filament, $\Delta\theta$, in terms of the limiting moduli E_H and E_L

$$\Delta\theta = \frac{3}{2}\frac{L^3}{t^2}\left(\frac{\chi}{\mu_0}B + M\right)\nabla B\frac{E_H - E_L}{E_H E_L}$$

Here, rather than anticipate any particular magnetic field geometry, we have assumed a constant magnetization state $\frac{\chi}{\mu_0}B + M$ over the range of motion. The range of a magnetically unsaturated device ($\mu_0 M \cong \chi B \ll \mu_0 M_{sat}$) that exhibits large deflection within a strong gradient will certainly be affected by changes in magnetization state over the course of deflection. However, the first-order scaling relations described by this function remain useful for device design. It is evident from this relationship, for example, that range of motion is maximized by choosing an SMP with a large variation in available moduli, and long, thin actuators will exhibit a greater range of motion.

For some applications, the torque available for the device to do work on its environment is more important than its range of motion. Available torque can be determined by considering the filament to be in its high-modulus equilibrium position as the elastic modulus shifts from E_H to E_L. In this case, the available torque, τ_A, is given by the difference between $\tau_E(E_H)$ and $\tau_E(E_L)$, at a deflection θ determined by $\tau_E(E_H) = \tau_M$, yielding

$$\tau_A = wtL^2\left(\frac{\chi}{\mu_0}B + M\right)\nabla B\frac{E_H - E_L}{E_H}$$

Thus, a thicker filament is able to exert more torque during an actuation cycle, even while its thickness limits the range of motion. Unsurprisingly, increasing the width of the actuator will increase the available torque without affecting range of motion, and both range and available torque scale with the product of magnetization and field gradient. Last, the total energy available to do work on the environment scales as the product of $\Delta\theta$ and τ_A. The appropriate design of a magnetic SMP will depend on its intended application, and these scaling relations provide guidance to that end.

For some applications, it may be important for an SMP device to remain highly unaffected by an applied magnetic field while in a high-modulus state yet respond strongly to the same field in its low-modulus state. We can define this characteristic as the "quality of actuation" Q, as shown below, where R is the ratio of magnetic torque to elastic torque per radian in the high-modulus (R_H) and low-modulus (R_L) states

$$Q = -\ln(R_H)\ln(R_L)$$

where $R_{H,L} = \frac{3}{2}\frac{L^3}{t^2}\left(\frac{\chi}{\mu_0}B + M\right)\frac{\nabla B}{E_{H,L}}$.

Q will be positive if and only if ($R_H < 1$ and $R_L > 1$) or ($R_H > 1$ and $R_L < 1$), that is, when the dominant torque switches from elastic to magnetic (or vice versa) upon heating. Furthermore, a greater degree of dominance of each respective torque will result in a higher Q so that

a high-Q system will be strongly dominated by elastic torque when cool and strongly dominated by magnetic torque when heated. A negative Q occurs when one torque (elastic or magnetic) dominates under both heated and cooled conditions; thus, a negative Q would represent a failed device. Further discussion of Q as applied to our DiAPLEX cantilever is available in the Supplementary Materials.

CONCLUSIONS

The use of MMPs in a bifunctional manner for simultaneous magnetic actuation and photothermal heating enables a new class of magnetically actuated, reconfigurable soft robots based on SMPs, where photothermal heating determines whether the SMP is locked or softens and allows reconfiguration. The shape memory effect further enhances the temporal programmability of these devices. In comparison with pneumatic actuation, remote stimulation with magnetic fields and light allows the use of simple untethered architectures that do not require a source of compressed air. We foresee the use of these materials for in vivo and aerospace applications, where tethering or use of compressed air could be challenging or impossible. These materials also have greater potential for microrobotics, where remote actuation becomes more important and fabrication of pneumatic soft microbots is also challenging. More broadly, this work highlights the potential for complex behaviors through coupling of orthogonal stimuli. In addition to reconfigurable cantilevers and scrolls, lifters highlight the potential of this material for practical applications, and snappers demonstrate control over the coupled magnetic and mechanical properties. The functionality of magnetic snappers is expanded by introducing biasing and shape memory. Simulations of the responses of cantilevers and snappers, including shape memory effects, closely align with experimental results, which suggests that the simulation framework may be used as a design tool for optimizing the function of soft robots before fabricating them. Future work will include improving the performance of these materials, customizing them to have different transition temperatures, and expanding their applications.

MATERIALS AND METHODS
Composite film preparation and characterization of cantilevers, flowers, scrolls, and snappers

Magnetic SMP films were prepared through solvent casting of thermoplastic polyurethane polymers, 0.5 g of IROGRAN (Huntsman Corporation, PS 455-203) or 0.2 g of DiAPLEX (SMP Technologies, MM5520), dissolved in 5 ml of tetrahydrofuran (THF) and stirred for at least 2 hours to completely dissolve the polymer pellets. Unless stated otherwise, masses of 0.05 g (for IROGRAN) or 0.02 g (for DiAPLEX) of carbonyl iron microparticles with an average diameter of 4.2 μm (MMPs, Jilin Jien Nickel Industry, JCF2-2) obtained from LORD Corporation were then added to the polymer solution and mixed uniformly with a vortexer. These masses were chosen to give a loading of 9.1 wt %, which is close to that used in our recent work (28). The mixture was poured into a rectangular polytetrafluoroethylene (PTFE) mold ($l = 7$ cm, $w = 2$ cm) for cantilevers, scrolls, and snappers and a circular PTFE mold ($d = 4.5$ cm) for flowers. For samples with chained magnetic particles used in cantilevers, scrolls, and snappers, the mold was placed between the poles of a GMW 3472-70 electromagnet in a horizontal field of 150 Oe immediately after pouring the solution. After solvent casting, the vertical segments at the edges of the film that adhered to the sides of the PTFE mold during solvent casting were removed with

scissors to obtain flat rectangular films. To further remove any residual THF in the films, the samples were annealed under ambient atmosphere. IROGRAN samples were annealed at 80°C for 10 min, and DiAPLEX samples were annealed at 120°C for 30 min. The thicknesses measured with a micrometer after allowing complete evaporation of the THF and annealing are 252 μm for the IROGRAN scrolls and snappers, 124 μm for the DiAPLEX cantilevers and scrolls, 142 μm for the DiAPLEX snappers, and 94 μm for the DiAPLEX flowers. The composite films were characterized by magnetometry [Quantum Design MPMS 3 superconducting quantum interference device (SQUID) vibrating sample magnetometer], scanning electron microscopy (FEI Verios 460L fieldemission scanning electron microscope with a secondary electron detector with an accelerating voltage of 1 kV), optical absorbance spectroscopy (Ocean Optics CHEMUSB4-VIS-NIR spectrophotometer), thermomechanical testing (TA Instruments RSA III), and differential scanning calorimetry (DSC) (PerkinElmer Diamond DSC).

Cantilever experiments
For photothermal heating, an Osram Golden DRAGON SFH 4750 LED with peak emission at 860 nm and power of 3500 mW was assembled in an aluminum housing with a longpass filter (Thorlabs, FGL780) taped to the front of the housing. DiAPLEX films with chained MMPs oriented along the length were cut into strips ($l = 3.3$ cm, $w = 0.5$ cm). Double-sided tape was used to mount one end of the strip to an inverted Petri dish, creating a cantilever with a length of 3.0 cm. A permanent magnet (1-inch-diameter, 0.5-inch-thick cylindrical NdFeB from Bunting Magnetics, N35P1000500) was held at a fixed height above the free end of the cantilever. The LED was oriented to illuminate the hinge at the fixed end of the cantilever. A Seek Thermal CompactPRO thermal imaging camera was used to record temperature changes in the film during photothermal heating.

Flower experiments
A circular PTFE mold ($d = 4.5$ cm) was used to prepare DiAPLEX films, which were solvent-cast in zero magnetic field. Scissors were used to manually cut six or eight radial, equally spaced wedges going 1.3 cm into the circular disc to define petals. The center of the sample was affixed to the center of a flat rotating stage with double-sided tape. The stage rotated at a speed of 0.9 rpm. The LED was placed above to illuminate the hinges of the petals before they were rotated beneath the permanent magnet. A permanent magnet (0.75-inch-diameter, 0.5-inch-thick cylindrical NdFeB from Bunting Magnetics, N35P7500500) was held at a fixed height above the edge of the sample such that the ends of the petals would pass beneath the magnet as the sample was rotated.

Scroll experiments
A rectangular strip of DiAPLEX ($l = 3.0$ cm, $w = 0.5$ cm) with the MMP chains oriented along its length was placed between two layers of aluminum foil, rolled into a scroll shape, and taped closed around a glass Pasteur pipette with an outer diameter of 4 mm. The foil and polymer film were placed in an oven at 180°C under vacuum for 6 hours to set the scroll as the permanent shape. IROGRAN scrolls were prepared in the same way, except with heating at 80°C for 30 min. The outer end of each scroll was affixed to a surface using double-sided tape. IROGRAN scrolls were manipulated by bringing a pair of stacked permanent magnets (0.5-inch-diameter, 0.5-inch-thick cylindrical NdFeB from Bunting Magnetics, N35P500500) near to the closed scroll, slowly pulling the stacked magnets away to extend the scroll, and then pulling them further away from the end of the extended scroll, causing it to close into

its permanent shape. DiAPLEX scrolls were manipulated using a permanent magnet (1-inch-diameter, 0.5-inch-thick cylindrical NdFeB from Bunting Magnetics, N35P1000500) held at a fixed distance from the scroll. The LED was placed on the other side of the scroll.

Snapper experiments

For experiments with unbiased DiAPLEX and biased and unbiased IROGRAN snappers, films ($l = 6.4$ cm, $w = 0.5$ cm) with the MMP chains oriented lengthwise were affixed with double-sided tape to a 3D-printed plastic frame (acrylonitrile butadiene styrene) in a buckled position such that the length of the film between the fixed ends was 4.8 cm and the end-to-end distance was reduced to 4.0 cm. Biased IROGRAN snappers were prepared by placing the film between two layers of aluminum foil and taping it in a buckled configuration, with each end anchored to a Petri dish and an end-to-end distance of 3.0 cm. Gravity caused the middle of the film to bow downward. The foil-wrapped IROGRAN film was placed in an oven at 80°C for 10 min to set the buckled configuration as the permanent shape. For preparing a biased DiAPLEX snapper, a rectangular strip of DiAPLEX polymer film ($l = 3.5$ cm, $w = 0.5$ cm) with 16.7 wt % loading of MMP chains oriented lengthwise was placed between two layers of aluminum foil and suspended with tape between two Petri dishes with an end-to-end distance of 1.5 cm to create a buckled configuration (fig. S6B). The foil and polymer film were placed in an oven at 180°C for 6 hours to set the buckled configuration as the permanent shape. At room temperature, the ends of the strip were pulled apart such that the end-to-end distance was 2.5 cm, and the strip was then affixed with double-sided tape to a 3D-printed plastic frame in a buckled configuration.

The frame was oriented vertically for all snapping experiments, orienting the snapper sideways and between permanent magnets (1-inch-diameter, 0.5-inch-thick cylindrical NdFeB from Bunting Magnetics, N35P1000500) or with a magnet to one side of the snapper, with the axis of the magnet orthogonal to the plane of the frame. For experiments with unbiased IROGRAN snappers, the frame was moved between the permanent magnets on both sides, driving the film to snap back and forth between the two buckled positions. For experiments with biased snappers, only one permanent magnet was placed on the side opposing the permanent buckled shape. For experiments with DiAPLEX snappers, a permanent magnet was placed on the side opposing the initial buckle in the film, and the LED was on the side adjacent to the buckle. Switching on the LED drove snapping. After an initial forward snap, for unbiased DiAPLEX snappers, the frame was then rotated 180° around a vertical axis to invert the orientation of the buckle. For biased DiAPLEX snappers, the frame was not rotated, but the magnet was removed. Switching the LED back on triggered a second snap. Two webcams were used to record optically driven DiAPLEX snappers.

Grabber experiments

A thicker film was used for the grabber than the other devices to make it more rigid. DiAPLEX (0.4 g) was dissolved in 10 ml of THF and poured into a circular PTFE mold ($d = 5$ cm) to prepare a DiAPLEX thin film by solvent casting (zero applied magnetic field). Scissors were used to define six tapered arms with a length of 1.6 cm and widths of 0.7 cm at the fixed end and 0.4 cm at the mobile end. Two hinges were manually folded in each arm at distances of 0.5 and 1.0 cm from the end to mimic phalanges and joints in human fingers. A small piece of a DiAPLEX film of thickness ~100 μm and with the same shape as the last segment with 28.6 wt % loading of MMPs was attached with double-sided tape on top of the last segment of each arm to enhance

the response to magnetic fields. To facilitate mounting and dismounting on the housing of the LED, a 3D-printed holder was constructed that held two glass slides separated by a gap of 3 mm, which reduced direct thermal heating of the grabber by the LED. One glass slide was attached to the LED, and the other was attached to the grabber. The blueberries used in the experiment have masses of 1.398 and 1.553 g, and the cherry tomatoes have masses of 3.161 and 3.166 g.

Simulations

Experimental results were corroborated with theoretical expectations by developing a numerical model of filament actuation, which is summarized here. Complete details are provided in the Supplementary Materials. In the model, the filament was treated as a thin elastic beam composed of 40 individual rigid segments. Because of the small size of each segment, each segment was treated as having a uniform magnetization and experiencing both a uniform magnetic field and a uniform magnetic field gradient, determined by its location relative to a simulated permanent magnet. The magnetization of the filament in the presence of a magnetic field gradient leads to an attractive magnetic force on each segment, favoring displacement toward the magnet. Elastic or gravitational forces may, however, restrict this motion. The net force on each segment of the filament due to magnetism, elasticity, and gravity (neglected for the snappers) determines the instantaneous acceleration of the filament in any configuration, from which its dynamics and equilibrium configurations may be determined.

Using an algorithm written in MATLAB R2017a, the field geometry in the neighborhood of the filament was first simulated, and then the net force on each segment of the filament was calculated. The net force was applied over a short time step to update the momentum of each segment, and the momentum was used to update the position of each segment over the same time interval. At each step, the momentum was reduced by a small fraction (0.1 to 0.5%) to dampen internal oscillations. This process was iterated until the average net force per segment fell below a minimum threshold value, which was set to 10 to 100 nN, depending on the system.

Elastic forces were modeled as two distinct components: bending and extension. Elastic bending forces were determined from Euler-Bernoulli beam theory under the assumption that each segment has a constant curvature. Elastic extension/compression forces always act parallel to the filament and are proportional to the modulus, cross-sectional area, and strain of each segment.

The magnetic field was taken to be that of an ideal cylindrical magnet and was modeled in the xy plane using an established algorithm (60). Each segment of the filament then attained a net volume magnetization according to the local field magnitude, where the magnetization curve of each of the materials, $M(B)$, has been measured (fig. S1). Differentiating the magnetic energy of each segment results in the net magnetic force, which depends on the local magnetic field magnitude, local magnetic field gradient, and the susceptibility of the filament, which was taken from the magnetization curves.

Dimensions of each modeled filament were chosen to match experimental configurations. The elastic modulus of IROGRAN at 25°C and the temperature-dependent elastic modulus of DiAPLEX were obtained from tensile testing of samples loaded with Fe particles (fig. S3). For modeling the shape memory behavior of DiAPLEX, its modulus was divided into two parts: The permanent configuration was assumed to have a fixed modulus equal to the minimum of $E(T) = E(80°C)$, while the temporary configuration had a temperature-dependent modulus comprising the remainder, or $E(T) - E(80°C)$.

SUPPLEMENTARY MATERIALS

Supplementary material for this article is available at http://advances.sciencemag.org/cgi/content/full/5/8/eaaw2897/DC1

REFERENCES AND NOTES

1. D. Trivedi, C. D. Rahn, W. M. Kier, I. D. Walker, Soft robotics: Biological inspiration, state of the art, and future research. *Appl. Bionics Biomech.* **5**, 99–117 (2008).

2. D. Rus, M. T. Tolley, Design, fabrication and control of soft robots. *Nature* **521**, 467–475 (2015).

3. C. Laschi, B. Mazzolai, M. Cianchetti, Soft robotics: Technologies and systems pushing the boundaries of robot abilities. *Sci. Robot.* **1**, eaah3690 (2016).

4. J. J. Mack, B. N. Cox, M. Lee, J. C. Y. Dunn, B. W. Wu, Magnetically actuable polymer nanocomposites for bioengineering applications. *J. Mater. Sci.* **42**, 6139–6147 (2007).

5. R. Fuhrer, E. K. Athanassiou, N. A. Luechinger, W. J. Stark, Crosslinking metal nanoparticles into the polymer backbone of hydrogels enables preparation of soft, magnetic field-driven actuators with muscle-like flexibility. *Small* **5**, 383–388 (2009).

6. R. M. Duffy, A. W. Feinberg, Engineered skeletal muscle tissue for soft robotics: Fabrication strategies, current applications, and future challenges. *Wiley Interdiscip. Rev. Nanomed. Nanobiotechnol.* **6**, 178–195 (2014).

7. Y. Liu, H. Du, L. Liu, J. Leng, Shape memory polymers and their composites in aerospace applications: A review. *Smart Mater. Struct.* **23**, 023001 (2014).

8. A. W. Hauser, A. A. Evans, J.-H. Na, R. C. Hayward, Photothermally reprogrammable buckling of nanocomposite gel sheets. *Angew. Chem. Int. Ed.* **54**, 5434–5437 (2015).

9. S. Shan, S. H. Kang, J. R. Raney, P. Wang, L. Fang, F. Candido, J. A. Lewis, K. Bertoldi, Multistable architected materials for trapping elastic strain energy. *Adv. Mater.* **27**, 4296–4301 (2015).

10. H. Meng, G. Li, Reversible switching transitions of stimuli-responsive shape changing polymers. *J. Mater. Chem. A* **1**, 7838–7865 (2013).

11. T. Takahashi, N. Hayashi, S. Hayashi, Structure and properties of shape-memory polyurethane block copolymers. *J. Appl. Polym. Sci.* **60**, 1061–1069 (1996).

12. R. Mohr, K. Kratz, T. Weigel, M. Lucka-Gabor, M. Moneke, A. Lendlein, Initiation of shape-memory effect by inductive heating of magnetic nanoparticles in thermoplastic polymers. *Proc. Natl. Acad. Sci. U.S.A.* **103**, 3540–3545 (2006).

13. G. M. Baer, W. Small IV, T. S. Wilson, W. J. Benett, D. L. Matthews, J. Hartman, D. J. Maitland, Fabrication and in vitro deployment of a laser-activated shape memory polymer vascular stent. *Biomed. Eng. Online* **6**, 43 (2007).

14. H. Zhang, J. Zhang, X. Tong, D. Ma, Y. Zhao, Light polarization-controlled shape-memory polymer/gold nanorod composite. *Macromol. Rapid Commun.* **34**, 1575–1579 (2013).

15. H. Zhang, Y. Zhao, Polymers with dual light-triggered functions of shape memory and healing using gold nanoparticles. *ACS Appl. Mater. Interfaces* **5**, 13069–13075 (2013).

16. F. H. Zhang, Z. C. Zhang, C. J. Luo, I.-T. Lin, Y. Liu, J. Leng, S. K. Smoukov, Remote, fast actuation of programmable multiple shape memory composites by magnetic fields. *J. Mater. Chem. C* **3**, 11290–11293 (2015).

17. B. K. Kim, S. Y. Lee, M. Xu, Polyurethanes having shape memory effects. *Polymer* **37**, 5781–5793 (1996).

18. Z. Ding, C. Yuan, X. Peng, T. Wang, H. J. Qi, M. L. Dunn, Direct 4D printing via active composite materials. *Sci. Adv.* **3**, e1602890 (2017).

19. A. Lendlein, Fabrication of reprogrammable shape-memory polymer actuators for robotics. *Sci. Robot.* **3**, eaat9090 (2018).

20. M. Behl, K. Kratz, J. Zotzmann, U. Nöchel, A. Lendlein, Reversible bidirectional shape-memory polymers. *Adv. Mater.* **25**, 4466–4469 (2013).

21. J. Zhou, S. A. Turner, S. M. Brosnan, Q. Li, J.-M. Y. Carrillo, D. Nykypanchuk, O. Gang, V. S. Ashby, A. V. Dobrynin, S. S. Sheiko, Shapeshifting: Reversible shape change in semicrystalline elastomers. *Macromolecules* **47**, 1768–1776 (2014).

22. M. D. Hager, S. Bode, C. Weber, U. S. Schubert, Shape memory polymers: Past, present and future developments. *Prog. Polym. Sci.* **49-50**, 3–33 (2015).

23. G. Z. Lum, Z. Ye, X. Dong, H. Marvi, O. Erin, W. Hu, M. Sitti, Shape-programmable magnetic soft matter. *Proc. Natl. Acad. Sci. U.S.A.* **113**, E6007–E6015 (2016).

24. W. Hu, G. Z. Lum, M. Mastrangeli, M. Sitti, Small-scale soft-bodied robot with multimodal locomotion. *Nature* **554**, 81–85 (2018).

25. S. R. Mishra, J. B. Tracy, Sequential actuation of shape-memory polymers through wavelength-selective photothermal heating of gold nanospheres and nanorods. *ACS Appl. Nano Mater.* **1**, 3063–3067 (2018).

26. J. Kim, S. E. Chung, S.-E. Choi, H. Lee, J. Kim, S. Kwon, Programming magnetic anisotropy in polymeric microactuators. *Nat. Mater.* **10**, 747–752 (2011).

27. S. R. Mishra, M. D. Dickey, O. D. Velev, J. B. Tracy, Selective and directional actuation of elastomer films using chained magnetic nanoparticles. *Nanoscale* **8**, 1309–1313 (2016).

28. M. M. Schmauch, S. R. Mishra, B. A. Evans, O. D. Velev, J. B. Tracy, Chained iron microparticles for directionally controlled actuation of soft robots. *ACS Appl. Mater. Interfaces* **9**, 11895–11901 (2017).

29. Y. Kim, H. Yuk, R. Zhao, S. A. Chester, X. Zhao, Printing ferromagnetic domains for untethered fast-transforming soft materials. *Nature* **558**, 274–279 (2018).

30. H.-W. Huang, T.-Y. Huang, M. Charilaou, S. Lyttle, Q. Zhang, S. Pané, B. J. Nelson, Investigation of magnetotaxis of reconfigurable micro-origami swimmers with competitive and cooperative anisotropy. *Adv. Funct. Mater.* **28**, 1802110 (2018).

31. S. Jiang, S. Hu, H. Wu, Y. Zhang, Y. Zhang, Y. Wang, Y. Zhang, W. Zhu, J. Li, D. Wu, J. Chu, Multifunctional Janus microplates arrays actuated by magnetic fields for water/light switches and bio-inspired assimilatory coloration. *Adv. Mater.* **31**, 1807507 (2019).

32. S. Maity, K. A. Kozek, W.-C. Wu, J. B. Tracy, J. R. Bochinski, L. I. Clarke, Anisotropic thermal processing of polymer nanocomposites via the photothermal effect of gold nanorods. *Part. Part. Syst. Charact.* **30**, 193–202 (2013).

33. R. J. G. Johnson, K. M. Haas, B. J. Lear, Fe₃O₄ nanoparticles as robust photothermal agents for driving high barrier reactions under ambient conditions. *Chem. Commun.* **51**, 417–420 (2015).

34. D. H. Yi, H. J. Yoo, S. S. Mahapatra, Y. A. Kim, J. W. Cho, The synergistic effect of the combined thin multi-walled carbon nanotubes and reduced graphene oxides on photothermally actuated shape memory polyurethane composites. *J. Colloid Interface Sci.* **432**, 128–134 (2014).

35. H. Koerner, G. Price, N. A. Pearce, M. Alexander, R. A. Vaia, Remotely actuated polymer nanocomposites—Stress-recovery of carbon-nanotube-filled thermoplastic elastomers. *Nat. Mater.* **3**, 115–120 (2004).

36. S. B. Abel, M. A. Molina, C. R. Rivarola, M. J. Kogan, C. A. Barbero, Smart polyaniline nanoparticles with thermal and photothermal sensitivity. *Nanotechnology* **25**, 495602 (2014).

37. T. Cantu, K. Walsh, V. P. Pattani, A. J. Moy, J. W. Tunnell, T. Betancourt, Conductive polymer-based nanoparticles for laser-mediated photothermal ablation of cancer: Synthesis, characterization, and in vitro evaluation. *Int. J. Nanomedicine* **12**, 615–632 (2017).

38. C. Chautems, A. Tonazzini, D. Floreano, B. J. Nelson, A variable stiffness catheter controlled with an external magnetic field. *IEEE/RSJ Int. Conf. Intell. Robots Syst.*, 181–186 (2017).

39. A. Espinosa, R. Di Corato, J. Kolosnjaj-Tabi, P. Flaud, T. Pellegrino, C. Wilhelm, Duality of iron oxide nanoparticles in cancer therapy: Amplification of heating efficiency by magnetic hyperthermia and photothermal bimodal treatment. *ACS Nano* **10**, 2436–2446 (2016).

40. X. Han, Z. Deng, Z. Yang, Y. Wang, H. Zhu, B. Chen, Z. Cui, R. C. Ewing, D. Shi, Biomarkerless targeting and photothermal cancer cell killing by surface-electrically-charged superparamagnetic Fe₃O₄ composite nanoparticles. *Nanoscale* **9**, 1457–1465 (2017).

41. M. Li, Y. Wang, A. Chen, A. Naidu, B. S. Napier, W. Li, C. L. Rodriguez, S. A. Crooker, F. G. Omenetto, Flexible magnetic composites for light-controlled actuation and interfaces. *Proc. Natl. Acad. Sci. U.S.A.* **115**, 8119–8124 (2018).

42. A. Crivaro, R. Sheridan, M. Frecker, T. W. Simpson, P. Von Lockette, Bistable compliant mechanism using magneto active elastomer actuation. *J. Intell. Mater. Syst. Struct.* **27**, 2049–2061 (2016).

43. H. Lee, C. Xia, N. X. Fang, First jump of microgel; actuation speed enhancement by elastic instability. *Soft Matter* **6**, 4342–4345 (2010).

44. J. U. Schmied, H. Le Ferrand, P. Ermanni, A. R. Studart, A. F. Arrieta, Programmable snapping composites with bio-inspired architecture. *Bioinspir. Biomim.* **12**, 026012 (2017).

45. E. G. Loukaides, S. K. Smoukov, K. A. Seffen, Magnetic actuation and transition shapes of a bistable spherical cap. *Int. J. Smart Nano Mater.* **5**, 270–282 (2014).

46. A. Firouzian-Nejad, S. Ziaei-Rad, M. Moore, Vibration analysis of bi-stable composite cross-ply laminates using refined shape functions. *J. Comp. Mater.* **51**, 1135–1148 (2016).

47. D. Yang, B. Mosadegh, A. Ainla, B. Lee, F. Khashai, Z. Suo, K. Bertoldi, G. M. Whitesides, Buckling of elastomeric beams enables actuation of soft machines. *Adv. Mater.* **27**, 6323–6327 (2015).

48. R. A. Bilodeau, E. L. White, R. K. Kramer, Monolithic fabrication of sensors and actuators in a soft robotic gripper. *2011 IEEE Int. Conf. Intell. Robots Syst.*, 2324–2329 (2015).

49. C. Laschi, M. Cianchetti, B. Mazzolai, L. Margheri, M. Follador, P. Dario, Soft robot arm inspired by the octopus. *Adv. Robot.* **26**, 709–727 (2012).

50. E. Brown, N. Rodenberg, J. Amend, A. Mozeika, E. Steltz, M. R. Zakin, H. Lipson, H. M. Jaeger, Universal robotic gripper based on the jamming of granular material. *Proc. Natl. Acad. Sci. U.S.A.* **107**, 18809–18814 (2010).

51. J. C. Breger, C. Yoon, R. Xiao, H. R. Kwag, M. O. Wang, J. P. Fisher, T. D. Nguyen, D. H. Gracias, Self-folding thermo-magnetically responsive soft microgrippers. *ACS Appl. Mater. Interfaces* **7**, 3398–3405 (2015).

52. E. Kizilkan, J. Strueben, A. Staubitz, S. N. Gorb, Bioinspired photocontrollable microstructured transport device. *Sci. Robot.* **2**, eaak9454 (2017).

53. W. Gao, L. Wang, X. Wang, H. Liu, Magnetic driving flowerlike soft platform: Biomimetic fabrication and external regulation. *ACS Appl. Mater. Interfaces* **8**, 14182–14189 (2016).

54. A. Cēbers, I. Javaitis, Bending of flexible magnetic rods. *Phys. Rev. E* **70**, 021404 (2004).

55. J. J. Abbott, O. Ergeneman, M. P. Kummer, A. M. Hirt, B. J. Nelson, Modeling magnetic torque and force for controlled manipulation of soft-magnetic bodies. *IEEE Trans. Robot.* **23**, 1247–1252 (2007).

56. P. von Lockette, S. E. Lofland, J. Biggs, J. Roche, J. Mineroff, M. Babcock, Investigating new symmetry classes in magnetorheological elastomers: Cantilever bending behavior. *Smart Mater. Struct.* **20**, 105022 (2011).

57. J. B. Tracy, T. M. Crawford, Magnetic field-directed self-assembly of magnetic nanoparticles. *MRS Bull.* **38**, 915–920 (2013).

58. F. Ilievski, A. D. Mazzeo, R. F. Shepherd, X. Chen, G. M. Whitesides, Soft robotics for chemists. *Angew. Chem. Int. Ed.* **50**, 1890–1895 (2011).

59. W. I. Small IV, P. Singhal, T. S. Wilson, D. J. Maitland, Biomedical applications of thermally activated shape memory polymers. *J. Mater. Chem.* **20**, 3356–3366 (2010).

60. N. Derby, S. Olbert, Cylindrical magnets and ideal solenoids. *Am. J. Phys.* **78**, 229–235 (2010).

Citation: J. A.-C. Liu, J. H. Gillen, S. R. Mishra, B. A. Evans, J. B. Tracy, Photothermally and magnetically controlled reconfiguration of polymer composites for soft robotics. *Sci. Adv.* **5**, eaaw2897 (2019).